

Droplets in an axisymmetric microtube: Effects of aspect ratio and fluid interfaces

A. C. DeVoria and K. Mohseni

Citation: *Physics of Fluids* (1994-present) **27**, 012002 (2015); doi: 10.1063/1.4904753

View online: <http://dx.doi.org/10.1063/1.4904753>

View Table of Contents: <http://scitation.aip.org/content/aip/journal/pof2/27/1?ver=pdfcov>

Published by the [AIP Publishing](#)

Articles you may be interested in

[On the levitation force in horizontal core-annular flow with a large viscosity ratio and small density ratio](#)

Phys. Fluids **25**, 032102 (2013); 10.1063/1.4793701

[Computational modeling of droplet based logic circuits](#)

AIP Conf. Proc. **1479**, 220 (2012); 10.1063/1.4756102

[Conveyor belt effect in the flow through a planar duct of a viscous fluid with spinning particles](#)

Phys. Fluids **24**, 083601 (2012); 10.1063/1.4745476

[Conveyor belt effect in the flow through a tube of a viscous fluid with spinning particles](#)

J. Chem. Phys. **136**, 164905 (2012); 10.1063/1.4707345

[A constitutive equation for droplet distribution in unidirectional flows of dilute emulsions for low capillary numbers](#)

Phys. Fluids **22**, 083301 (2010); 10.1063/1.3466577



Droplets in an axisymmetric microtube: Effects of aspect ratio and fluid interfaces

A. C. DeVoria¹ and K. Mohseni^{1,2,a)}

¹*Department of Mechanical and Aerospace Engineering, University of Florida, Gainesville, Florida 32611, USA*

²*Department of Electrical and Computer Engineering, University of Florida, Gainesville, Florida 32611, USA*

(Received 4 April 2014; accepted 5 December 2014; published online 6 January 2015)

The flow within a liquid droplet steadily translating along an axisymmetric microtube is investigated experimentally and compared with a model to predict the invariants of the flow, that is circulation, hydrodynamic impulse, and kinetic energy. The model is based on pipe Poiseuille flow and allows for variable aspect ratio, \mathcal{R} . The invariants are computed from the velocity fields, which are measured with micro digital particle image velocimetry. The non-dimensionalized experimental invariants show negligible dependence on the Reynolds number, within the small range investigated (~ 1.5 – 13), which also agrees with the model. The effect of introducing a fluid interface is found to increase the observed magnitude of invariants in low- \mathcal{R} droplets above those in continuous flow. Also increased are the average rates at which invariants are advected across a hypothetical flux plane within the tube. The increase in these rates above continuous flow goes as \mathcal{R}^{-1} . The momentum flux is similarly increased for low- \mathcal{R} and is mainly attributed to the converging/diverging radial velocities near the trailing/leading interfaces. The momentum flux is also compared with available synthetic jet data. © 2015 AIP Publishing LLC. [<http://dx.doi.org/10.1063/1.4904753>]

I. INTRODUCTION

A class of multi-phase flow that has received increasing attention is that of Taylor (or segmented) flows¹ in which individual packets of fluid are manipulated and transported through microchannels. This type of flow consists of two immiscible fluids that appear in an orderly train of alternating droplets/bubbles. Most often the two fluids are a liquid (droplet) phase and a gas phase. Fairbrother and Stubbs² used bubbles of air separating a viscous liquid to study how the presence of thin films affect the expected mass flow rate in the microchannel. Taylor³ continued to investigate the two-phase flow and proposed a set of possible streamlines that depicted two counter-rotating vortices (relative to a reference moving with the droplet) around the axis of symmetry. This flow field has been verified by several researchers.^{4–6}

The circulating flow within droplets, both immersed in another fluid as well as confined to a channel, has been well-documented in theoretical,^{7,8} experimental,^{9–13} and computational^{14,15} works and is known to enhance transport/mixing capabilities. Typical applications involving droplet flows are monolith reactors,¹⁶ lab-on-a-chip diagnostics,¹⁷ and thermal management systems.^{15,18–20} In such microsystems, surface tension forces are dominant and so low-energy actuation methods, such as electrowetting and laser forcing, may be efficiently utilized. Droplets/bubbles can also modify the flow external to them, such as in flow nucleate boiling. Recently, Houshmand and Peles²¹ experimentally studied the introduction of air bubbles into a liquid microchannel heater. Under certain conditions, they observed an enhanced heat transfer coefficient (compared to single-phase flow), which is attributed to the acceleration of the carrier liquid around the air bubbles.

^{a)} Author to whom correspondence should be addressed. Electronic mail: mohseni@ufl.edu

Also important to microfluidic applications is the formation processes used to generate droplets or bubbles. Recently, Duxenneuner *et al.*²² investigated the formation of droplets via liquid-liquid dispersion (injection) with both Newtonian and non-Newtonian fluids as the immersed phase. Using micro digital particle image velocimetry (μ -DPIV) they measured the flow both inside the forming droplets as well as outside in the continuous phase. The formation process is observed to depend on the flow rates and the viscoelasticity of the immersion phase, resulting in substantially different detachment dynamics. Another common droplet/bubble formation technique is the use of T- and Y-junctions (e.g., Refs. 13, 23, and 24). Chaoqun *et al.*²⁴ studied the formation of carbon dioxide bubbles with deionized water slugs at high Reynolds numbers ($\sim 10^2$) common to industrial applications. As a result of non-negligible inertial effects, the bubble formation frequency is increased due to the detachment dynamics being governed by the momentum of the liquid phase.

Regardless of the formation process, a very important parameter that can have a significant effect on the utility of droplets/bubbles for a given application is the associated aspect ratio, \mathcal{A} . The radial velocity within droplets, which is responsible for the circulating flow, results from the introduction of a fluid interface. In this paper, we investigate a two-phase flow in a microtube (a fully wetting water droplet with air on either side). The aim is to elucidate basic fluid physics that pertain to applications that are perhaps less conventional than those typically associated with Taylor flows. Specifically, we consider the effects that the droplet interfaces have on various fluid dynamic quantities, such as circulation, hydrodynamic impulse, and kinetic energy. Moreover, the droplet quantities are compared with those corresponding to continuous pipe flow to provide insight into advantages of droplet flows over continuous ones. In particular, applications that employ microjets will typically benefit from increased momentum and energy fluxes, which are possibly realized using droplet flows. For example, fuel injectors employing droplet flows could achieve larger spreading rates, and so more efficient mixing, if more momentum and energy can be introduced into the droplets prior to their ejection through the spray nozzle.

The effect of a circulating flow in a droplet is fairly intuitive: a radial velocity results in wall-normal convection. The other invariants can provide further metrics by which the usefulness of a droplet may be gauged. As an application, consider the transport of solid particles in a liquid through a microchannel. Although the flow is circulating, it possible that these particles may prematurely settle out (e.g., due to gravitational effects). In this case, the kinetic energy may better describe the ability of the liquid to retain the particles in the rotating fluid. A major issue in many microchannel devices, particularly those with chemical reactions, is clogging of the pathways with particles, reagents, contaminants, etc.²⁵ Kohler and Cahill²⁵ briefly discuss flushing the channels as a method to maintain/restore proper operation of the device. A liquid droplet could be employed for this purpose, and here the hydrodynamic impulse can represent how effective the droplet is in unclogging the channel. In other words, the impulse is a measure of how intensely the droplet will impact the clogged area and thus how well it may loosen and remove undesired materials.

This manuscript is organized as follows. In Sec. II, the particular problem under investigation is briefly discussed. The details of the experimental setup are given in Sec. III. Section IV presents a model to predict the total amounts of circulation, hydrodynamic impulse, and kinetic energy in the droplets. Next in Sec. V, the experimental results are shown and compared with the model in various ways. Section V D discusses the momentum flux of the droplets and is compared to synthetic jet data in Sec. V E.

II. PROBLEM DESCRIPTION

In microfluidic applications, it is common to refer to the carrier fluid as a slug and the immersed phase as a droplet or bubble depending on whether it is a liquid or gas, respectively. Under this nomenclature, the current experiments consist of a liquid slug surrounded by a gas. However, since only a single slug is investigated, we refer to this liquid as a droplet. Also, it should be noted that these experiments have dry tube wall conditions.

The droplet has an axial length L and translates at a constant velocity U in a circular microtube of diameter D . L is defined as the distance along the tube centerline between the trailing and

leading interfaces. We use cylindrical coordinates with position vector $\mathbf{x} = (r, \phi, x)^T$ describing the radial, azimuthal, and axial directions, respectively. The corresponding velocity components are $\mathbf{u} = (v, w, u)^T$. The droplet aspect ratio is $\mathcal{R} = L/D$ and values of 1, 1.5, and 2 are investigated. The Reynolds number is defined as $Re = UD/\nu$, with ν being the kinematic viscosity of the droplet fluid, and is varied from ~ 1.5 to ~ 13 . The capillary number is $Ca = \mu U/\gamma$, where μ is the dynamic viscosity of the droplet fluid and γ is the interface surface tension; the associated range of Ca is $1.02 \times 10^{-5} - 7.72 \times 10^{-5}$.

The small values and ranges of Re and Ca are a result of experimental constraints. As such, it should be kept in mind that the results are only verified for cases of slower-moving droplets, where inertial effects are negligible relative to viscous effects, which in turn are less important than capillary effects. Also, since the same working fluid and tube diameter are used, then $Re \propto Ca$ and so their changes are accomplished through varying U .

III. EXPERIMENTAL SETUP AND TECHNIQUES

To quantitatively measure the velocity field within the droplet, we use μ -DPIV.^{26–28} The experimental setup is shown schematically in Fig. 1(a) and consists of a diode-pumped solid state laser (AIXIZ Gam1000B) with 1 W of 532 nm wavelength continuous output and an upright microscope (Olympus BX41) coupled to a high-speed CMOS camera (Phantom v210) that has a sensor resolution of 1280×800 pixel². The infinity-corrected objective (Olympus Plan N) has a magnification $M = 4$ and numerical aperture $NA = 0.1$. The channel is a circular glass tube with inner diameter $D = 2.34$ mm and wall thickness of 0.83 mm. An expression for the depth of field (δz) of a microscope objective is given by Inoué and Spring,²⁹ while one for the depth of correlation ($2z_{\text{corr}}$) is given by Olsen and Adrian.³⁰ For the current optical setup, these quantities are $\delta z/D = 0.046$ and $2z_{\text{corr}}/D = 0.121$. Hence, there will be some underestimation of the velocity measurements, but it is not expected to be significant (see Sec. V).

Droplets are injected manually using a 25 μL precision syringe (Hamilton #702). Given the camera sensor size, D , and M , only droplets of a particular size can fit entirely within the field of view. Droplet sizes of 15, 20, and 25 μL are investigated and correspond to droplet aspect ratios of approximately 1, 1.5, and 2, respectively. The length of the droplet, L , is defined as the length between the trailing and leading menisci and is used to determine \mathcal{R} . The droplets are pressure driven using a syringe pump (Chemyx Fusion 200) that allows for specified flow rates. For each case

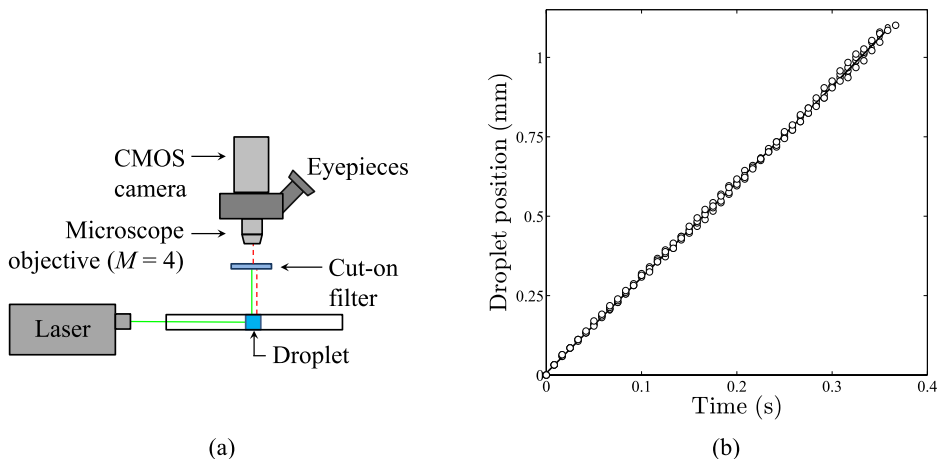


FIG. 1. (a) Schematic of the μ -DPIV setup. The laser beam (solid green line) is steered down the axis of the tube and the cut-on filter passes the emission of the fluorescent particles (dashed red line). The camera is coupled to the microscope; only the head and eyepieces of the microscope are shown. (b) The measured droplet position as a function of time obtained from the whole-image correlation for 5 different runs. For all cases, each run has a correlation coefficient with $R^2 > 0.9990$ and the standard deviation of the 5 slopes is $O(10^{-2})$ mm/s.

(i.e., prescribed flow rate), 5 independent data sets are acquired. The inter-frame time of the camera is set so that the largest expected velocity (estimated from Poiseuille flow) will approximately satisfy the $\frac{1}{4}$ rule.³¹

The working fluid is de-ionized water and is seeded with 3.2 μm diameter fluorescent polystyrene particles (Thermo Scientific) that are neutrally buoyant (1.06 g/cm³). An optical filter (Andover Corp.) with a cut-on wavelength of 550 nm and 5% transmission at 542 nm is placed in-line to reject scattered light and pass the fluoresced emission of the particles (70 nm Stokes shift). The curved surface of the droplets creates some scatter that is intense enough to pass through the filter. However, this did not significantly affect the quality of the particle images within the droplets.

To reduce the effects of imaging through curved surfaces of different media, the glass tube is placed through a small rectangular acrylic box which is then filled with water. The indexes of refraction for water and the glass tube are $n_w = 1.33$ and $n_g = 1.46$, respectively, giving a ratio of $n_w/n_g = 0.91$. A ray tracing calculation yields that the error between the image and object positions for this optical setup is negligible with a maximum error of only 1.7% at 97.5% of the radius. Beyond this total internal reflection occurs, meaning that the apparent tube wall in the image is actually $0.0125D$ away from it.

The droplets are allowed to translate at least 15 diameters before measurements are taken to ensure steady flow, which is corroborated in the $\mu\text{-DPIV}$ measurements. In the movies captured by the camera, the droplet translates across the field of view. However, since the flow is steady, the images are shifted to a reference image so that the droplet appears stationary. This is accomplished by letting the first image in the sequence serve as a reference to which all subsequent ones are shifted and is done in image pairs so as to maintain the particle shift. The scattered light from the surface of the droplet serves as a constant identifiable “mark” in the image and allows for the droplet position to be determined from a one-dimensional, whole-image correlation. Figure 1(b) shows the time-dependent droplet position for the 5 runs of a typical case. As expected, the relation is linear and the slope gives the bulk translational velocity of the droplet.

Figure 2(a) shows an image of the $\mathcal{R} = 1$ droplet as illuminated by the microscope light. The shape of the droplet is interesting with a nearly spherical meniscus at the rear interface caused by the driving pressure, whereas the leading interface is almost planar. These interface shapes are due to an appreciable interfacial pressure jump at the trailing interface and a near-zero jump value at the leading interface. However, the droplet is visually observed to maintain axial symmetry. This is also supported by the gravitational Bond number $Bo = \rho g R^2 / \gamma = 0.18 < 1$, which represents the ratio of gravitational-to-surface tension forces. The $\mathcal{R} = 1.5$ and 2 droplets exhibit similar interfaces. Figure 2(b) shows an example of the average of the overlaid, shifted images where the particle images essentially create a streak photography effect, qualitatively identifying the circulating flow.

The shifted particle images are processed using the INSIGHT 4GTM software from TSI, Inc. Since the particle density is necessarily low for $\mu\text{-DPIV}$ experiments,³² the images (about 40-100 per run depending on \mathcal{R}) are processed using the correlation averaging technique developed by

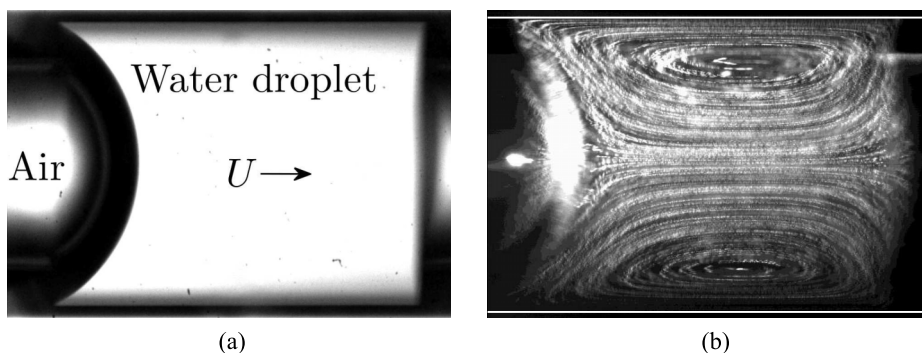


FIG. 2. (a) Image of a $\mathcal{R} = 1$ droplet illuminated by the microscope light. The droplet is moving from left to right. (b) The average of the shifted images; the thick white lines indicate the tube wall. The image has been processed to enhance contrast for visual purposes only.

Meinhart *et al.*²⁸ A multi-pass algorithm with window shifting and deformation is used. Since the flow has a major axial component, the interrogation windows are set to be rectangular beginning with 64×32 pixel² (3 passes) and decreasing to 32×16 pixel² (2 passes) with 50% overlap. This yields DPIV spatial resolutions of $0.035D \times 0.017D$ in the axial and radial directions, respectively.

IV. ANALYTICAL MODEL

Here, we discuss a simple model for the flow in a droplet translating in a channel. The main objective is to obtain estimates of the invariants of the motion, that is, the circulation, Γ , hydrodynamic impulse, I , and kinetic energy, E . For an axisymmetric flow, these quantities may be expressed by the following integrals:

$$\Gamma = \iint \omega r dr dx, \quad I = \rho\pi \iint r^2 \omega r dr dx, \quad E = \rho\pi \iint (u^2 + v^2) r dr dx. \quad (1)$$

Using the tube diameter, D , and the bulk velocity of the droplet, U , as length and velocity scales, we define the associated non-dimensional quantities as

$$\Gamma^* = \frac{\Gamma}{UD}, \quad I^* = \frac{I}{\rho U D^3}, \quad E^* = \frac{E}{\rho U^2 D^3}, \quad (2)$$

where ρ is the droplet fluid density. Although the flow within a translating droplet is most generally three-dimensional, it is often axisymmetric, which suggests that the well-known analytical solution for pipe Poiseuille flow may be of some value. In this regard, we model the droplet of aspect ratio $\mathcal{R} = L/D$ as a cylindrical slug of fluid in which the velocity is everywhere equal to the Poiseuille profile. For this reason, we refer to this model as the ‘‘Poiseuille slug.’’ Note that our usage of the term ‘‘slug’’ is slightly different from convention, which defines a slug to have a uniform velocity; by specifying a velocity distribution, we uniquely set the values of the invariants. The non-dimensional invariants are³³

$$\Gamma^* = 2\mathcal{R}, \quad I^* = \frac{\pi}{4}\mathcal{R}, \quad E^* = \frac{\pi}{6}\mathcal{R}. \quad (3)$$

Equations (3) are obtained by substituting the pipe Poiseuille profile, i.e., $u_p = 2U(1 - 4r^2/D^2)$, into Eqs. (1) where the axial integration is over $x/D = 0 \rightarrow \mathcal{R}$. Although this flow cannot exist physically, it can be interpreted to represent a segment of continuous flow comparable to the droplet.

Note that although this model has introduced the concept of an interface through a variable \mathcal{R} , it has ignored the significant radial velocity near the interfaces in real, finite- \mathcal{R} droplets. However, the effect of \mathcal{R} on the droplet circulation may be qualitatively observed by assuming that the radial velocity is constant and equal to some multiple, say k , of U . Then the line integral (of velocity) along the center-line of the droplet and the interfaces gives the non-dimensional circulation as

$$\Gamma^* = \frac{(2U)L + (kU)(D/2) + (-kU)(-D/2)}{UD} = 2\mathcal{R} + k. \quad (4)$$

Note that if the interface has non-zero curvature, then the circulation velocity must be that which is tangential to the surface. References 15 and 34 have used a similar analysis while investigating the heat transfer capabilities of droplets. Those works have indicated that $k < 1$. Hence, for low- \mathcal{R} droplets both terms on the far right-hand side are expected to have comparable contributions to the circulation. In reality, the center-line velocity may differ from Poiseuille flow and so the factor of 2 could be replaced by another constant; however, the dependence on \mathcal{R} is clear.

For a given \mathcal{R} , the above model predicts the *non-dimensional* invariants to be constant for *different dimensional* parameters (i.e., different U and D). Next, we use the μ -DPIV data to investigate how the above model compares with the measured invariants.

V. RESULTS

First, the assumption of axisymmetric flow is verified directly using the μ -DPIV measurements. Namely, for such a flow the mean axial velocity, which is equal to the droplet bulk velocity, may be

calculated as

$$U = \frac{1}{A} \iint u dA = \frac{2}{R^2} \int_0^R ur dr, \quad (5)$$

where A is the cross-sectional area and R is the tube radius. Using the measurements to compute Eq. (5) recovers U to 95% on average; this slight underestimate is expected due to the depth of correlation effects associated with μ -DPIV.^{30,35}

A. Flow field quantities

With the axisymmetric assumption valid, the azimuthal vorticity, ω , is the only non-zero component and is computed from the data using central differences. Figure 3 shows examples of vorticity fields with the corresponding velocity field relative to the droplet superimposed. Similar flow fields were obtained for all cases. Of note is the intense vorticity generation near the triple-contact points particularly at the trailing interface where the contact angle is less than 90° . This will have the tendency to increase the total circulation within the droplet. Conversely, there are boundary layers on the surface of the spherical rear interface creating opposite-sign vorticity to that of the main vortex structures. At higher Ca and/or Re , these boundary layers will grow and result in a secondary pair of counter-rotating vortices (similar to the separation zone behind a sphere). For example, Dore *et al.*²³ observed secondary vortices in the water droplets of a liquid-liquid slug flow in a circular microchannel at $Ca \sim O(10^{-2})$ and $Re \sim O(10^{-1})$, and Meyer *et al.*³⁶ observed similar vortices in the air bubbles of a gas-liquid Taylor flow in a square microchannel at $Ca \sim O(10^{-1})$ and

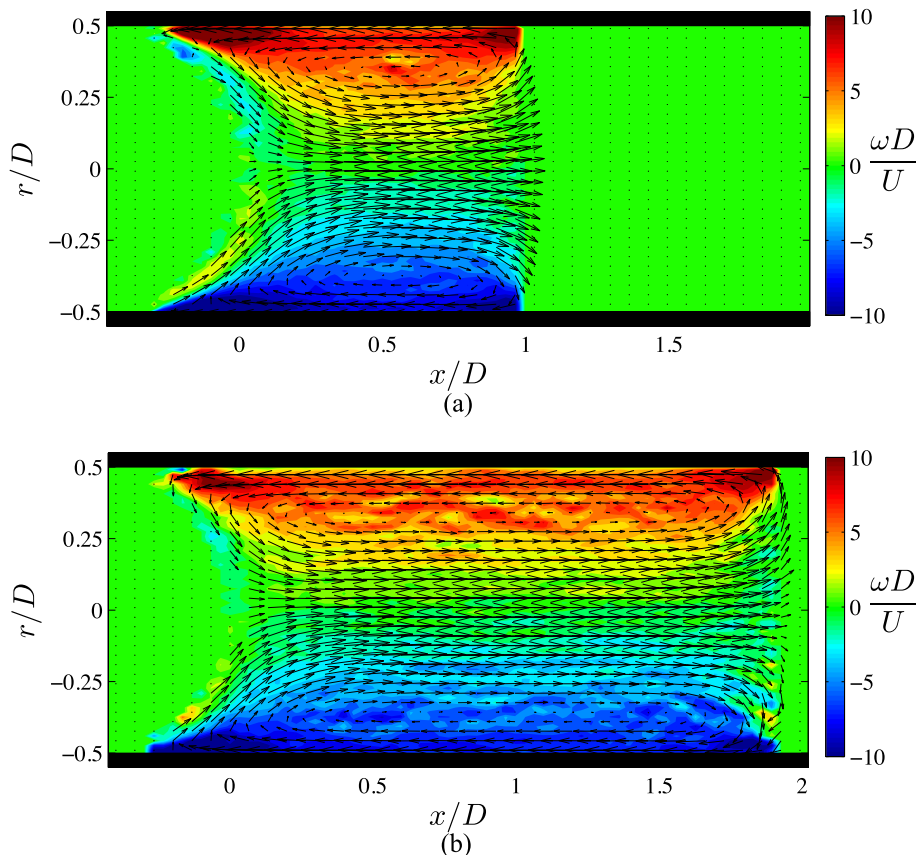


FIG. 3. Typical vorticity fields overlaid with velocity vectors relative to the moving droplet for (a) $\mathcal{R} = 1$ and (b) $\mathcal{R} = 2$. The solid black represents the tube wall. For each case $Re \approx 6.5$; similar vorticity fields were obtained for $\mathcal{R} = 1.5$ and all other Re cases. For clarity, the vector spacing is twice the spacing of the μ -DPIV data.

$Re \sim O(10)$. These vortices are of practical importance as they can be used to facilitate separation of solid particles from the carrier fluid in solid handling applications.²⁵

Another interesting feature observed in Fig. 3 is that, away from the triple-contact points, the vorticity at the interfaces is nearly zero. In fact, upon closer inspection the velocity field near the interfaces is similar to potential stagnation point flow. Since such a flow is irrotational, the context under which the radial velocity was ignored for the circulation and hydrodynamic impulse in the Poiseuille slug model is strengthened. However, the kinetic energy would have a contribution from this flow; see Eqs. (1).

To assess the deviation of the measured velocity from Poiseuille flow, Fig. 4 plots axial and radial velocity profiles at different axial positions along the $\mathcal{R} = 1$ and 2 droplets. Baird and Mohseni¹⁵ showed similar velocity profiles in their computations of a two-dimensional droplet in a parallel plate channel. Not surprisingly, the axial velocity at the axial center of the droplets ($x \approx 0.5L$) is essentially that of pipe Poiseuille flow. Near the interfaces the peak axial velocity is reduced with a flatter top-hat-like segment in the center portion of the droplet. This is because the axial velocity on the actual interface must be U . However, the profiles near the trailing and leading interfaces ($x \approx 0.03L$ and $0.96L$) show that the approach of the velocity toward the value U is asymmetric about the axial center. Also, at the trailing interface the velocity actually initially increases from the centerline value, which is attributed to the acute contact angle. For $\mathcal{R} = 1$, these features are more pronounced.

The radial velocity in the center of the droplet is zero, again suggesting that the flow there is Poiseuille flow. The profiles at the interfaces are more similar (equal and opposite) as might be expected from the *total* radial momentum necessarily equaling zero in an axisymmetric flow. We can now estimate the circulation contribution coming from the velocity on the interface as discussed in Sec. IV (see Eq. (4)). This velocity must be that which is projected tangentially onto the surface; in general the surface has non-zero curvature. Although the axial velocity of the interface is U , in the reference frame moving with the droplet this velocity is zero, however the total circulation remains unaffected. In other words, this contribution can be absorbed into those from the circuit segments along the center-line and the wall when in the moving reference frame.

Opting to make calculations in the moving reference frame leaves the integral of the radial velocity as in Eq. (6). However, here the integration is with respect to the variable r_s , which is the value of the radial coordinate as the interface surface is traced out (see Fig. 5(b)).³⁷

$$\Gamma_I = \int_0^{D/2} v(r_s) dr_s, \quad (6)$$

where Γ_I is the circulation contribution from one interface. Figure 5(a) plots the experimental radial velocity on the curved trailing surface as a function of r_s and shows that the profile is approximately sinusoidal with amplitude $|v/U| \equiv k\pi$; adopting such a form and substituting into Eq. (6) gives

$$\Gamma_I^* = \frac{\Gamma_I}{UD} = \frac{k\pi}{D} \int_0^{D/2} \sin(2\pi r_s/D) dr_s = k. \quad (7)$$

Figure 5 gives a representative value of $k\pi \approx 0.3$ for each \mathcal{R} , and so the estimated contribution from the curved trailing interface is $\Gamma_{TI}^* \approx 0.095$. Directly evaluating Eq. (6) with the experimental data yields $\Gamma_{TI}^* \approx 0.090, 0.094, \text{ and } 0.093$ for the $\mathcal{R} = 1, 1.5, \text{ and } 2$ cases, respectively. Note that Eq. (7) could also be used for the nearly planar leading interface since the velocity profiles are approximately sinusoidal as well, and $r_s \rightarrow r$. Despite these positive contributions from the interfaces, the reduction in the droplet center-line velocity from the Poiseuille flow value ($=2U$) means that the $2\mathcal{R}$ contribution to the circulation will be similarly reduced. These two competing effects are likely dependent on \mathcal{R} .

The vorticity distributions are shown in the bottom row of Fig. 4. The experimental distribution follows the Poiseuille profile as expected, but near the interfaces the vorticity sharply increases. As mentioned in the discussion of Fig. 3, this corresponds to the intense vorticity by the triple-contact points. Similarly, the flatter vorticity profile in the radial center portion of the droplet represents the low magnitude vorticity region. Again, these features are more pronounced for the $\mathcal{R} = 1$ droplet.

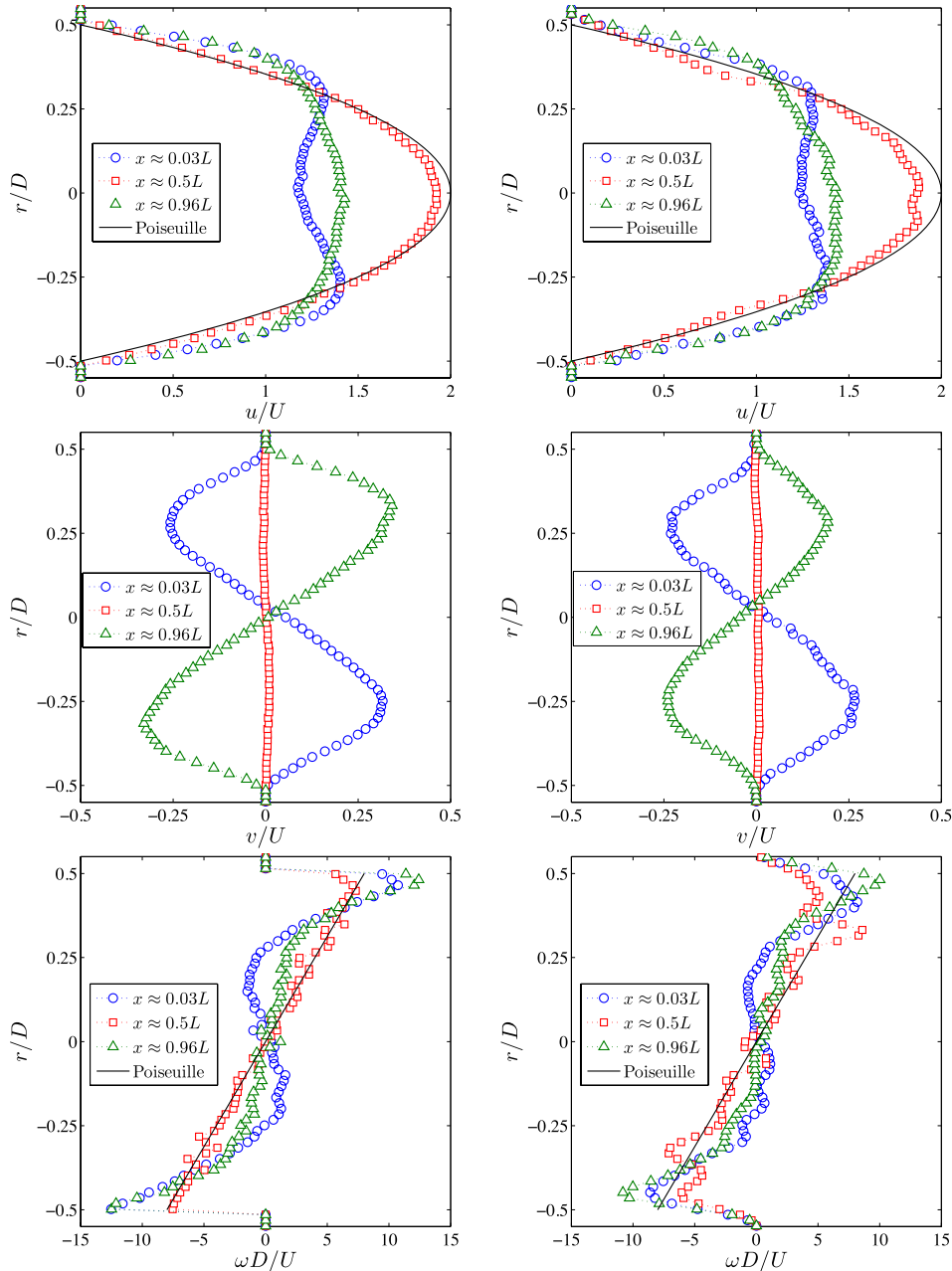


FIG. 4. Vertical profiles of the axial velocity (top), radial velocity (middle), and vorticity (bottom) for droplets with $\mathcal{R} = 1$ (left) and $\mathcal{R} = 2$ (right). Also shown are the corresponding Poiseuille profiles as indicated. These data are for the $Re \approx 8.3$ cases for each \mathcal{R} .

B. Experimental comparison of invariants

The circulation, hydrodynamic impulse, and kinetic energy are computed from Eqs. (1). This is done for each of the 5 independent runs for a given case so that statistical information can be obtained. Note that the velocity in the kinetic energy integral must be in an inertial (lab) reference frame; the vorticity remains unchanged.

Equations (3) suggest that the non-dimensional invariants will be proportional to \mathcal{R} , and so we divide the experimental data by the corresponding droplet aspect ratios in an attempt to further collapse the data. Figure 6 plots these data versus Reynolds number. This figure shows that the

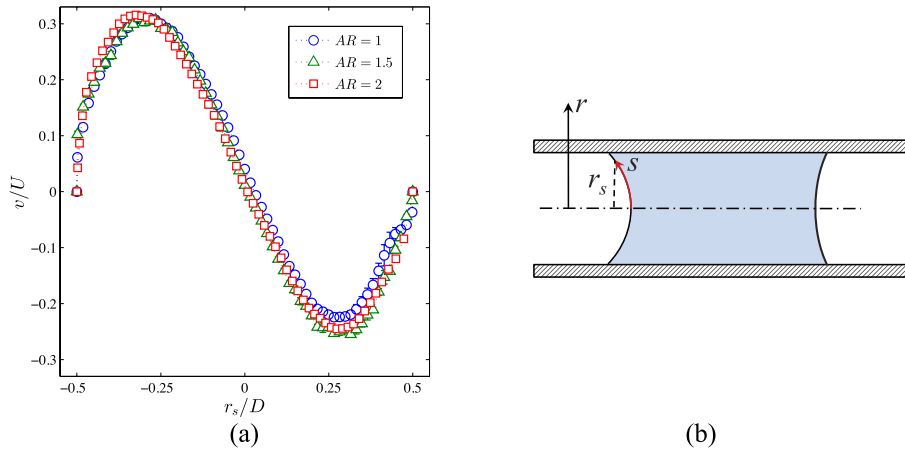


FIG. 5. (a) The radial velocity component on the curved trailing interface surface for all AR cases. Note that these data are not on a single radial line. (b) Schematic defining r_s as the radial coordinate of the curve along the interface that has a surface coordinate s .

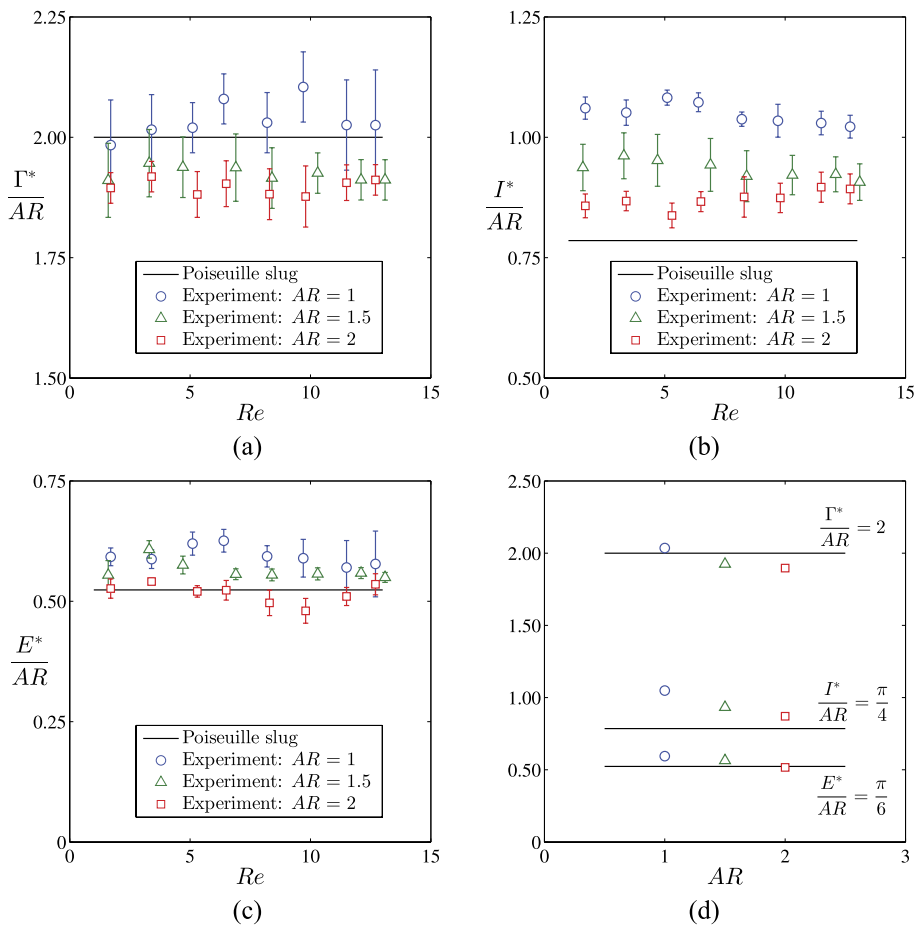


FIG. 6. The non-dimensional invariants divided by AR : (a) circulation, Γ^* , (b) hydrodynamic impulse, I^* , and (c) kinetic energy, E^* . For each plot the vertical axis range is the same. (d) The invariants as functions of aspect ratio; the experimental data are obtained as the average across all Re cases. The lines correspond to the Poiseuille slug model for all plots as indicated.

Poiseuille slug provides fair predictions of the droplet invariants. Additionally, there is no observable dependence on Re , which agrees with the model. On the other hand, it should be recalled that the range of Re investigated is limited and so no universal claims can be made. The model gives more accurate predictions for the circulation and kinetic energy (Figs. 6(a) and 6(c)). However, for the hydrodynamic impulse (Fig. 6(b)) there is more noticeable variation with \mathcal{R} .

The effects of droplet aspect ratio may be better assessed by plotting the experimental invariants (again divided by \mathcal{R}) as functions of aspect ratio, as shown in Fig. 6(d). The plot reveals that there is a generally decreasing trend in the invariants with increasing \mathcal{R} . Also, for low- \mathcal{R} , the invariants are increased above the Poiseuille flow values. In other words, this suggests that bringing the interfaces closer together (i.e., decreasing \mathcal{R}) has the effect of increasing the circulation, hydrodynamic impulse, and kinetic energy within a droplet. Although the range of \mathcal{R} tested is small, these data still indicate that the droplet flow and the associated invariants quickly approach continuous pipe flow with increasing \mathcal{R} (>2).

For the circulation, the Poiseuille slug model initially under-predicts Γ^* , but then over-predicts for larger \mathcal{R} . This is because the model assumes the vorticity at any point is non-zero (except at $r = 0$). However, recall from Fig. 3 that the measurements show a low-magnitude vorticity field near the droplet interfaces and opposite-sign boundary layer vorticity on the curved rear interface. These features will reduce the circulation in the droplet. Conversely, the intense vorticity near the triple-contact points will have the opposite effect. For the hydrodynamic impulse, the model under-predicts I^* , which can be explained in a similar manner by examining the second of Eqs. (1). The integrand is weighted with r^2 so that the vorticity in the “corners,” where $r \approx D/2$, will have a more significant contribution to the integral than that from the low-magnitude vorticity field near the interfaces.

The kinetic energy is well-predicted for all three \mathcal{R} 's despite that the droplets have an axial velocity that decreases from the Poiseuille profile as the interfaces are approached (Fig. 4 top row) as well as a radial velocity. For the sake of simplicity, consider the difference between the Bernoulli “constants” for the droplet and the Poiseuille slug,

$$-\frac{1}{2}\rho(u_p^2 - u^2) + \frac{1}{2}\rho v^2 + (P - P_p), \quad (8)$$

where u_p and P_p are the Poiseuille axial velocity and pressure. Since the same pressure gradient would be employed to establish each flow, we can assume $(P - P_p) \approx 0$. Then it is possible that the decrease in kinetic energy associated with the axial velocity (first term) is balanced by the contribution from the radial velocity (second term), resulting in near-zero energy difference.

C. Flux of invariants

For piston-cylinder vortex rings Krieg and Mohseni³⁸ showed that the amounts and injection rates of invariants are significantly increased by the presence of a non-zero radial velocity at the nozzle exit plane. Figure 4 showed that the droplets have a significant radial velocity near the interfaces. In fact, the velocity profiles in Fig. 4 are similar to those presented in Krieg and Mohseni³⁸ for the velocities at the nozzle exit plane (see Figs. 8 and 11 of Ref. 38). Section V B has shown that the Poiseuille slug model provides a somewhat reasonable prediction of the *total* amounts of invariants in a droplet. However, the model cannot provide insight into the reasons why discrete droplets have been observed to have advantages over continuous flows,^{20,34,39} including the results of the current experiments, which have shown an increase in the total invariants for low- \mathcal{R} droplets.

Similar to the nozzle exit plane of a piston-cylinder mechanism, we consider a “flux plane” in the tube through which the droplets pass as shown in Fig. 7. However, note that this hypothetical flux plane is distinctly different because the droplets just continue to translate along the tube and are not ejected into an ambient fluid. Figure 8 plots the amount of invariants that have crossed the flux plane as a function of non-dimensional time $t^* \equiv Ut/D$. Also shown are the amounts corresponding to continuous Poiseuille flow. Note that $t^* = x/D$ since the droplet is steadily translating, and the “unsteadiness” is only due to the convection of invariants as seen by a stationary observer at the flux plane.

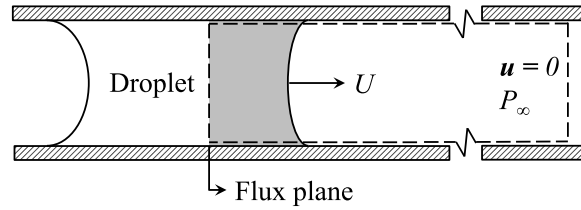


FIG. 7. Schematic of a droplet crossing through the flux plane in the tube. The shaded portion of the droplet is the integration region used to obtain the time-dependent invariants. The dashed lines indicate the closed control surface which extends to infinity where the velocity is zero and the pressure is the ambient.

For $\mathcal{R} = 1$, the amounts and rates-of-change (slopes) of the invariants are increased above continuous Poiseuille flow. When the droplet has almost entirely crossed the flux plane, the rates decrease because of the opposite-sign vorticity on the trailing interface which represents a negative contribution to the invariants. Additionally, the non-zero contact angle, which causes the curvature of the interface (see Fig. 3), means there is less fluid crossing the flux plane at these times. For $\mathcal{R} = 2$, the experimental data are much more consistent with the continuous flow because as \mathcal{R} increases the velocity in the main portion of the droplet tends to the Poiseuille profile (recall Fig. 4).

The experimental data in Fig. 8 are used to compute an average rate-of-change of the invariants. Figure 9 plots the percent increases of the average experimental rates above those for continuous Poiseuille flow. For low- \mathcal{R} droplets, which are most common in applications, the increase of the rates is appreciable. For example, with $\mathcal{R} = 1$, the increases in the rates of Γ^* , I^* , and E^* are about 11, 23, and 20%, respectively. However, there is hardly any increase by $\mathcal{R} = 2$. The curves in Fig. 9 are least-squares fits using a \mathcal{R}^{-1} form as suggested by the jet model of Xia and Mohseni⁴⁰ (see Sec. V E), which shows that this trend with \mathcal{R} is indeed plausible for the droplets.

In typical applications, a steady train of discrete droplets is utilized rather than a single droplet. Also, the secondary phase (gas) will create finite gaps between the liquid droplets and the unit of periodicity becomes one pair of the liquid-gas phases. The spacing between droplets is often expressed through the liquid fraction, n . If we consider the gas phase to have a negligible contribution to the flux of invariants, then the results presented in Fig. 9 are still applicable if an effective aspect ratio is defined as $\mathcal{R}_{\text{eff}} \equiv \mathcal{R}/n$, where \mathcal{R} is again the liquid droplet aspect ratio. The value of n decreases from unity in the ideal, no gap case. Therefore, a gap between droplets increases \mathcal{R}_{eff} and according to Fig. 9 will decrease the associated invariant fluxes. This provides an alternate

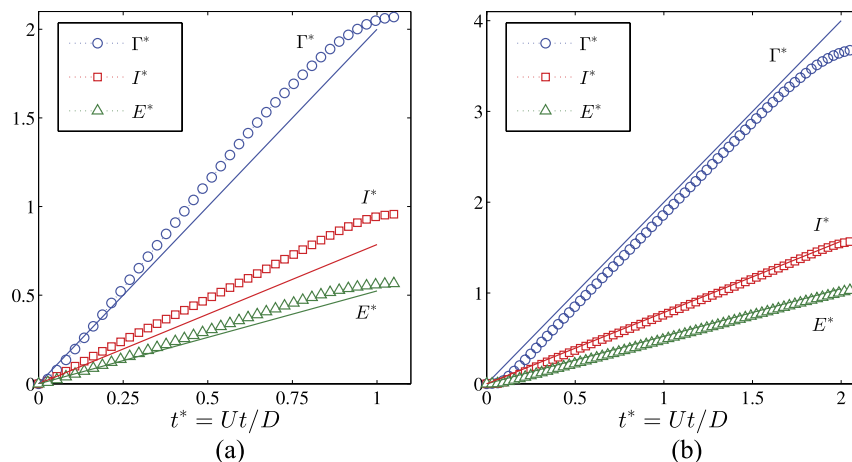


FIG. 8. The amount of invariants that have passed through the flux plane (see Fig. 7) as a function of time for (a) $\mathcal{R} = 1$ and (b) $\mathcal{R} = 2$. The solid lines are the corresponding estimates from continuous Poiseuille flow.

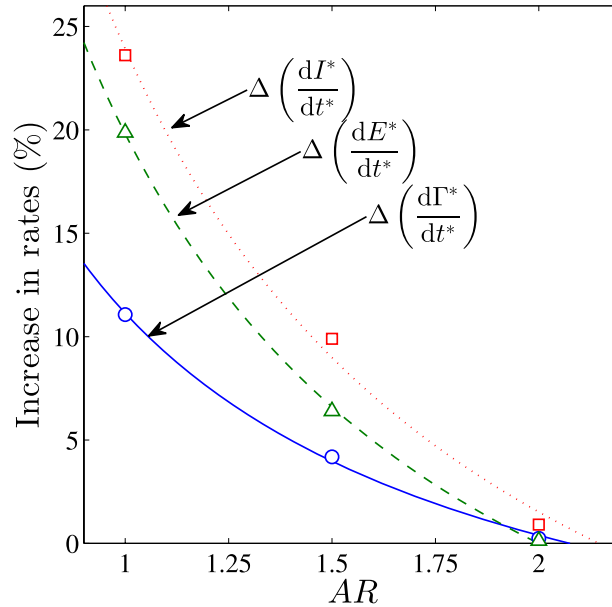


FIG. 9. The percent increase in the average flux of invariants for the experimental droplets (symbols) above continuous Poiseuille flow. The lines correspond to curves fit to the data using the form $c_0 + c_1 AR^{-1}$ suggested by the synthetic jet normalization.

explanation for the use of high-frequency pulsed microjets in applications such as inkjet printing and microsurgery. Namely, the high frequency pulsation implies closely spaced packets of fluid (i.e., droplets) that contain more momentum and energy than a comparable segment of a continuous jet. For inkjet printing, this improves the accuracy of print placement while maintaining high printing speeds.⁴¹ For microsurgery, this allows the pulsed microjets to make very precise incisions with minimal damage to surrounding tissues.³⁹

D. Momentum flux

Another important quantity, which is closely related to the invariants, is the momentum flux. Here we present and discuss some results concerning this quantity. Technically, the flux plane is one boundary of a closed control surface; the other boundaries are the tube wall and another plane, which is supposed to be at an infinite axial location in the tube where the velocity/vorticity are zero and the pressure is the ambient, P_∞ (see Fig. 7). Following similar arguments as in Krieg and Mohseni³⁸ and defining $H(t)$ to be the total amount of axial momentum that has passed through the flux plane by time t , we then have

$$H = \rho \int_V u dV, \quad (9)$$

$$\frac{dH}{dt} = 2\rho\pi \int u^2 r dr + 2\pi \int [P(r) - P_\infty] r dr - 2\pi R\mu \int \omega dx. \quad (10)$$

The first integral term on the right-hand side is the usual flux of axial fluid momentum. In the second integral, $P(r) - P_\infty \equiv \Delta P$ is often termed the “over-pressure”^{38,42} at the flux plane. The third integral represents the viscous flux of momentum via diffusion of vorticity across the tube wall, where μ is the dynamic viscosity. As the center portion of the droplet crosses the flux plane, the flow is basically Poiseuille flow (recall Fig. 4), and so the rate at which axial momentum crosses the flux plane will be nearly constant as it is for the Poiseuille slug. Hence, when compared to continuous flow, we can see why increasing the droplet AR does not provide an increase in the *time-averaged* fluxes. However, near the interfaces we must directly consider the second and third integral terms in Eq. (10).

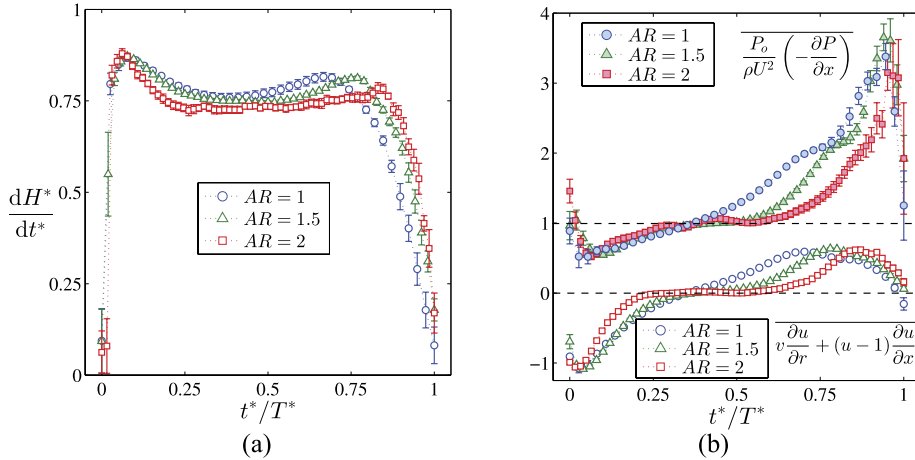


FIG. 10. (a) The non-dimensional momentum flux for each \mathcal{R} case. The time t^* is normalized by the time taken for the entire droplet to cross the flux plane, $T^* \approx \mathcal{R}$. (b) The spatial average over the tube cross-section of the non-dimensional convective acceleration and the pressure gradient at the flux plane. For each plot and \mathcal{R} , the data are the average across all Re cases from which the error bars are determined.

Figure 10(a) plots the non-dimensional momentum flux for each \mathcal{R} , where time is normalized by that taken for the entire droplet to cross the flux plane, $T^* (\approx \mathcal{R})$. When the nearly planar leading interface passes through the flux plane there is a sharp increase in the flux, which then relaxes to a fairly constant value as discussed above. Then as the trailing interface is approached, there is a slight rise in the flux, followed by a sharp decrease as the actual curved interface surface passes. The fluxes for the different \mathcal{R} are generally collapsed on this time-scale, because it accounts for the length of the droplet. However, the momentum flux magnitude is slightly higher with decreasing \mathcal{R} (before the sharp decrease).

The work of Krieg and Mohseni³⁸ has shown that the radial velocity in jets will create an appreciable ΔP that is maintained over most of the ejection time, whereas for parallel jets the over-pressure goes to zero after the initial vortex formation process completes. We can extrapolate these concepts to interpret the expected behavior of ΔP for the droplets. Namely, the converging/diverging streamlines near the trailing/leading interface may be thought of as a jet with significant radial velocity that accelerates/decelerates the fluid into/from the center portion of the droplet where the flow is like a parallel jet. This explains the behavior of the fluxes as discussed in the previous paragraph, where the “humps” seen in the fluxes are caused by the radial velocity contributions associated with the over-pressure at the interfaces.

Although we could determine the integrated pressure contribution to the momentum flux by computing the other terms in Eq. (10), it proves to be more insightful to proceed along a different avenue, as is shown next. Namely, we revert the integral transformations that led to Eq. (10) and return to the (differential) equation for the conservation of axial momentum, which as a consequence of the steady translation, can be written in *non-dimensional* form as

$$v \frac{\partial u}{\partial r} + (u-1) \frac{\partial u}{\partial x} = \frac{P_o}{\rho U^2} \left(-\frac{\partial P}{\partial x} \right) + \frac{1}{Re} \nabla^2 u, \quad (11)$$

where $P_o/(\rho U^2)$ is the characteristic pressure scale, and all other quantities are understood to be non-dimensional; ∇^2 is the Laplacian operator in cylindrical coordinates. When the left-hand side of Eq. (11) is zero, the pressure gradient is exactly that required to balance the loss of momentum due to viscous action, as it is in Poiseuille flow. We now use the experimental data to compute the average of the convective acceleration and the viscous term over the cross-section of the tube (i.e., $\frac{2\pi}{\pi R^2} \int [\] r dr$), and in the remainder of this discussion these average quantities, which represent force per-unit-length of the droplet, are implied. The convective acceleration is plotted in Fig. 10(b) against t^*/T^* . Initially there is a negative peak as the leading interface passes which represents the deceleration of the axial velocity as it approaches this interface. There is clearly an asymmetry in

this term as the droplet crosses the flux plane, which is more apparent for lower \mathcal{R} . Namely, it seems that the closer the interfaces are, the more the axial flow is accelerated. This result is certainly a contributor to the increased momentum flux as well as the invariant fluxes for low- \mathcal{R} droplets.

Now, physical reasoning yields $P_o/(\rho U^2) \propto Re^{-1}$ since the flow is pressure-driven. However, the fact that the convective accelerations show little variation with Re (via narrow error bars in Fig. 10(b)) implies this dependency can be absorbed into the viscous term. It should be remarked that an explicit Reynolds number dependence is more than likely to be present at larger values of Re than those studied here. For this purpose, we define a scaling coefficient for the viscous term, say $\alpha > 0$, such that the product of $P_o/(\rho U^2)$ and the non-dimensional pressure gradient is arbitrarily equal to unity when the left-hand side of Eq. (11) is zero. Then α is determined from the requirement that

$$0 = -1 + \frac{\alpha}{Re} |\nabla^2 u|_0, \quad (12)$$

where the subscript “0” denotes a specific value of this term. In effect, α re-scales the viscous term so that when Eq. (11) is rearranged to compute the pressure gradient term, its value will have significance with regard to the left-hand side of Eq. (11). The data for (minus) the pressure gradient are also plotted in Fig. 10(b), and note that it is indeed ~ 1 when the convective acceleration is zero. Again, this integrated term is the average pressure-force per-unit-length and is clearly not constant as in Poiseuille flow. In fact, as the trailing edge is approached, the peak in the force density is significantly higher than that at the leading interface and indicates the highly concentrated force at the triple-contact line.⁴³ Alternatively, consider the pressure gradients required to generate the intense vorticity in these locations. Note that the penetration depth of this force into the droplet is increased for low- \mathcal{R} . Since the leading interface is almost planar and the trailing interface is curved, it would seem that the difference in these force density peaks is associated with the different contact angles.

E. Flux of numerous droplets: Application to synthetic jets

The periodicity associated with a train of discrete droplets in a microtube can also be used to draw parallels to jetting applications, in particular pulsed synthetic jets. Jets are typically characterized by a few different metrics such as the spreading rate, the decay of axial velocity, and the axial momentum flux. Since the droplets in the current experiments are not actually ejected from the tube, we can only estimate the momentum flux using the data of Sec. V D, which is based on the rate at which momentum passes through the hypothetical flux plane. However, the spreading and decay rates are closely related to the momentum flux.

Figure 10(a) showed that the momentum flux was increased as droplet \mathcal{R} is decreased, or equivalently as the introduction of fluid interfaces are more closely spaced. Although apparently only a slight increase, when considering the flux of numerous droplets, the accumulated effect could be advantageous. Conceptually, this is similar to pulsed water jets used for rock cutting, which are generated by an impacting piston.^{44,45} Fig. 11 illustrates the potential benefit of using a sequence of low- \mathcal{R} droplets to generate a pulsed jet, where the dashed line represents a constant reference value for each \mathcal{R} . For the $\mathcal{R} = 1$ droplet, the increase above this reference value coupled with the larger frequency of droplets crossing the flux plane in a given time results in an increased average momentum flux. This hypothetical “jet” is based on the assumption that the data for a single droplet may be periodically repeated to represent a real train of droplets. Figure 12(a) shows a schematic comparing the amount of fluid ejected by a conventional synthetic jet and by a droplet jet; the near-field flow is purposely not represented.

It is conventional to denote the average momentum flux of a jet as K , which we now adopt. The momentum flux for synthetic jets, K_{sj} , is typically non-dimensionalized as

$$K_{sj}^* = \frac{K_{sj}}{\rho D^4 f^2}, \quad (13)$$

where f is the driving frequency of the actuator (e.g., membrane, plunger), D is the orifice diameter, and ρ is the fluid density as before. Also, a classic slug flow model with uniform, time-dependent

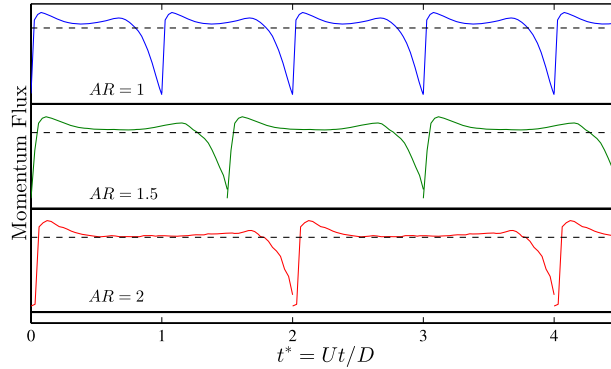


FIG. 11. The momentum flux of a hypothetical train of droplets: the data for a single droplet is repeated periodically. (Top) $AR = 1$, (middle) $AR = 1.5$, and (bottom) $AR = 2$. For each case, the thick black line is the abscissa and the dashed lines are a common reference value.

ejection velocity is usually defined using f such that the stroke ratio of the actuator is L/D , which is equivalent to the aspect ratio of the ejected fluid during one cycle. The slug velocity is typically chosen to be sinusoidal with a 50% duty cycle in order to model the oscillatory motion of the actuator velocity program.^{40,46} In accordance with Eq. (13), the non-dimensional momentum flux of the slug model is $K_s^* = (\pi^3/16)AR^2$.

Now, in order to compare the momentum flux of the droplets to that of synthetic jets, we need to determine an equivalent frequency for the former, f_d . Using the sinusoidal actuator velocity we obtain $f_d = 2U/(\pi L) = 2U/(\pi D AR)$. The jet model of Xia and Mohseni⁴⁰ further normalizes the non-dimensionalization of Eq. (13) by K_s^* . Following this model and substituting f_d in Eq. (13) yields

$$\frac{K_d^*}{K_s^*} = \frac{4}{\pi} \left[\frac{K_d}{\rho D^2 U^2} \right] \propto \frac{1}{AR}, \tag{14}$$

where the term in square brackets is the non-dimensionalization that is in compliance with Eq. (2) and was previously used for the invariants and in Sec. V D. Accordingly, this yields the proportionality to AR^{-1} and suggests that the fluxes of the other invariants have a similar behavior (see Fig. 9).

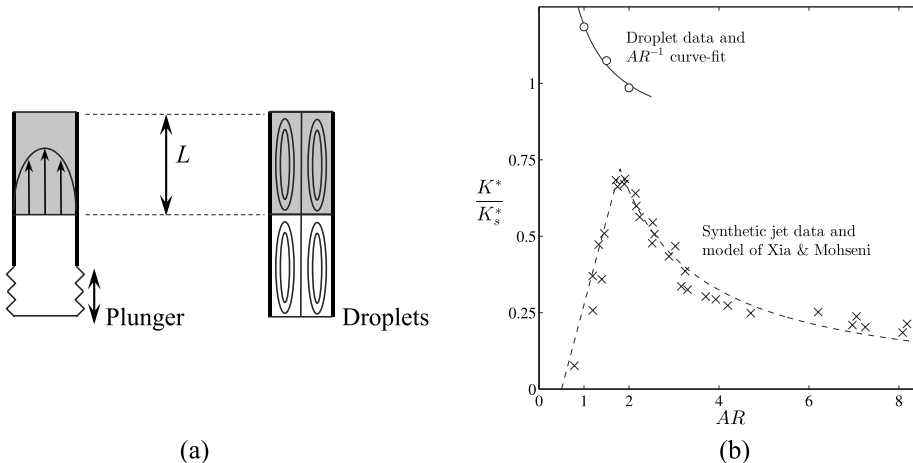


FIG. 12. (a) Schematic comparing the fluid ejected by a synthetic jet with an oscillating plunger (left) and a jet comprised of droplets (right). The near-field flow topology is not represented. The hypothesized benefit of the droplet jet is an increased momentum flux due to the fully developed vortical flow in the droplets. (b) The droplet momentum flux normalized as in Eq. (14) (open symbols) and a AR^{-1} curve-fit (solid line). Also shown is the flux from the synthetic jet data of Xia and Mohseni⁴⁰ (cross symbols) and the corresponding jet model (dashed line).

Figure 12(b) plots the momentum flux of the droplets as in Eq. (14), as well as the high frequency synthetic jet data and model of Xi and Mohseni.⁴⁰ The model curve (dashed line) is a piece-wise function, where the scaled momentum flux scales linearly with \mathcal{R} for values below ~ 1.8 . This value is the limiting stroke ratio, which is analogous to the vortex formation number for piston-cylinder-like mechanisms ($L/D \approx 4$) at which the leading vortex ring is at maximum strength.⁴⁷ Above $\mathcal{R} = 1.8$, the vorticity is distributed in such a way that corresponds to a decreased momentum flux, and goes as \mathcal{R}^{-1} , which agrees with the droplet trend. However, the droplet data show an increase of momentum flux and a continuation of a \mathcal{R}^{-1} trend for $\mathcal{R} < 1.8$. Although this situation is rather idealized, these results suggest that a droplet jet may bypass the vortex formation at the exit plane to obtain a higher momentum flux. In other words, the fluid that is ejected is already a fully developed vortical flow at maximum strength and does not rely on the shear layer roll-up process at the exit plane.

Smith and Swift⁴⁸ report that synthetic jets have higher spreading rates than continuous jets but are “slower” because of larger amounts of entrained fluid in the near field. Hence, the introduction of a fluid interface may allow synthetic jets to obtain near-field velocities more comparable to continuous jets, while maintaining a larger spreading rate. As a particular example, fuel injectors could achieve faster mixing rates by injecting discrete droplets, which would improve fuel consumption efficiency.

VI. CONCLUDING REMARKS

The flow within droplets translating at steady velocity through an axisymmetric microtube was investigated to provide insight on the related effects of fluid interfaces, droplet aspect ratio, and radial velocity. A simple model was considered to predict the flow invariants (circulation, hydrodynamic impulse, and kinetic energy). The model is termed the Poiseuille slug and is a cylindrical slug of fluid with the velocity field everywhere equal to the pipe Poiseuille profile. Also, the model indicates that the non-dimensional invariants are independent of Re . The Poiseuille slug allows for variable \mathcal{R} and predicts the invariants to have a linear relation to \mathcal{R} . However, the significant radial velocity observed in real droplets is neglected in this model.

Quantitative measurements of the flow inside the droplets were made with μ -DPIV. Droplet aspect ratios of 1, 1.5, and 2 were investigated, and for each \mathcal{R} , the Reynolds number ranged from 1.5 to 13 and the capillary number ranged from 1.02×10^{-5} to 7.72×10^{-5} . For a given \mathcal{R} , the flow fields (velocity and vorticity) were similar for each Re . As suggested by the models, the measured invariants showed no major dependence on Re , however the range of Re investigated was fairly limited. The Poiseuille slug satisfactorily captured the experimental trend of the invariants with \mathcal{R} . The advantage of using finite- \mathcal{R} droplets was evaluated by considering the average rate at which invariants cross a hypothetical flux plane within the tube. It was shown that low- \mathcal{R} droplets inject invariants at higher rates compared to continuous flow. The increase of these rates above continuous flow goes as \mathcal{R}^{-1} and is attributed to the fact the fluid interfaces are then more closely spaced. As expected, these rates are decreased as the spacing between droplets is made larger.

The axial momentum flux of the droplets was also considered. The significant radial velocities near the droplet interfaces were shown to create an over-pressure contribution to the momentum flux. Alternatively, the induced velocity of the intense vorticity near the triple-contact points accelerates the fluid in the center portion of the droplet. For low- \mathcal{R} , these effects are more pronounced and lead to an increase in the momentum flux, and is a result of the fact that the fluid interfaces are closer together. The average force per-unit-length was found to sharply increase at the interfaces and is associated with a concentrated force at the triple-contact line. This force can cause pinning (stiction) and affects the amount of input energy required to move a droplet (the experiments had dry tube wall conditions).

The momentum flux of the droplets was also compared to some available data for synthetic jets. It was assumed that a train of discrete droplets is approximated by periodically repeating a single droplet. In this way, it was implied that the droplets had increased fluxes at lower \mathcal{R} . A possible application to synthetic jets is that the introduction of a fluid interface, prior to the ejection

of fluid, will allow the jet to obtain higher axial velocities in the near field while maintaining a high spreading rate.

Future work may include expanding the limited experimental ranges of \mathcal{R} and especially Re and Ca , as well as experiments which eject droplets from a nozzle into an ambient fluid.

ACKNOWLEDGMENTS

This work is supported by grants from the Office of Naval Research and from the National Science Foundation through the Thermal Transport Processes program.

- ¹ In some heat transfer applications, this type of two-phase flow has also been referred to as “digitized heat transfer.”
- ² F. Fairbrother and A. Stubbs, “119. Studies in electro-endosmosis. Part VI. The “bubble-tube” method of measurement,” *J. Chem. Soc.* **1935**, 527–529
- ³ G. Taylor, “Deposition of a viscous fluid on the wall of a tube,” *J. Fluid Mech.* **10**, 161–165 (1961).
- ⁴ B. Cox, “An experimental investigation of the streamlines in viscous fluid expelled from a tube,” *J. Fluid Mech.* **20**, 193–200 (1964).
- ⁵ T. Thulasidas, M. Abraham, and R. Cerro, “Flow patterns in liquid slugs during bubble-train flow inside capillaries,” *Chem. Eng. Sci.* **52**, 2947–2962 (1997).
- ⁶ A. Günther, S. Khan, M. Thalmann, F. Trachsel, and K. Jensen, “Transport and reaction in microscale segmented gas–liquid flow,” *Lab Chip* **4**, 278–286 (2004).
- ⁷ M. Hill, “On a spherical vortex,” *Philos. Trans. R. Soc., A* **185**, 213–245 (1894).
- ⁸ J. Hadamard, “Mouvement permanent lent d’une sphere liquide et visqueuse dans un liquide visqueux,” *C. R. Acad. Sci.* **152**, 1735 (1911).
- ⁹ K. Spells, “A study of circulation patterns within liquid drops moving through a liquid,” *Proc. Phys. Soc. B* **65**, 541–546 (1952).
- ¹⁰ J. McDonald, “The shape and aerodynamics of large raindrops,” *J. Meteorol.* **11**, 478–494 (1954).
- ¹¹ T. Horton, T. Fritsch, and R. Kintner, “Experimental determination of circulation velocities inside drops,” *Can. J. Chem. Eng.* **43**, 143–146 (1965).
- ¹² H.-W. Lu, F. Bottausci, J. Fowler, A. Bertozzi, C. Meinhart, and C.-J. Kim, “A study of EWOD driven droplets by PIV investigation,” *Lab Chip* **8**, 456–461 (2008).
- ¹³ M. Oishi, H. Kinoshita, and M. Oshima, “Simultaneous measurement of internal and surrounding flows of a moving droplet using multicolour confocal micro-particle image velocimetry (micro-PIV),” *Meas. Sci. Technol.* **22**, 1–13 (2011).
- ¹⁴ S. Hodges, O. Jensen, and J. Rallison, “The motion of a viscous drop through a cylindrical tube,” *J. Fluid. Mech.* **501**, 279–301 (2004).
- ¹⁵ E. Baird and K. Mohseni, “Digitized heat transfer: A new paradigm for thermal management of compact micro-systems,” *IEEE Trans. Compon. Packag. Technol.* **31**, 143–151 (2008).
- ¹⁶ M. Kreutzer, F. Kapteijn, J. Moulijn, and J. Heiszwolf, “Multiphase monolith reactors: Chemical reaction engineering of segmented flow in microchannels,” *Chem. Eng. Sci.* **60**, 5895–5916 (2005).
- ¹⁷ H. Stone, A. Stroock, and A. Ajdari, “Engineering flows in small devices: Microfluidics toward a lab-on-a-chip,” *Annu. Rev. Fluid Mech.* **36**, 381–411 (2004).
- ¹⁸ P. Walsh, E. Walsh, and Y. Muzychka, “Heat transfer model for gas–liquid slug flows under constant flux,” *Int. J. Heat Mass Transfer* **53**, 3193–3201 (2010).
- ¹⁹ A. Betz and D. Attfanger, “Can segmented flow enhance heat transfer in microchannel heat sinks?,” *Int. J. Heat Mass Transfer* **53**, 3683–3691 (2010).
- ²⁰ A. Asthana, I. Zinovik, C. Weinmueller, and D. Poulikakos, “Significant nusselt number increase in microchannels with a segmented flow of two immiscible liquids: An experimental study,” *Int. J. Heat Mass Transfer* **54**, 1456–1464 (2011).
- ²¹ F. Houshmand and Y. Peles, “Impact of flow dynamics of the heat transfer of bubbly flow in a microchannel,” *J. Heat Transfer* **136**(2), 022902 (2013).
- ²² M. Duxenneuner, P. Fischer, E. Windhab, and J. Cooper-White, “Simultaneous visualization of the flow inside and around droplets generated in microchannels,” *Microfluid Nanofluid* **16**, 743–755 (2014).
- ²³ V. Dore, D. Tsaoulidis, and P. Angeli, “Mixing patterns in water plugs during water/ionic liquid segmented flow in microchannels,” *Chem. Eng. Sci.* **80**, 334–341 (2012).
- ²⁴ Y. Chaoqun, Z. Yuchao, Y. Chunbo, D. M. an D. Zhengya, and C. Guangwen, “Characteristics of slug flow with inertial effects in a rectangular microchannel,” *Chem. Eng. Sci.* **95**, 246–256 (2013).
- ²⁵ J. Köhler and B. Cahill, *Micro-Segmented Flow* (Springer, 2014), Chap. 6.
- ²⁶ J. Santiago, S. Wereley, C. Meinhart, and R. Adrian, “A particle image velocimetry system for microfluidics,” *Exp. Fluids* **25**, 316–319 (1998).
- ²⁷ C. Meinhart, S. Wereley, and J. Santiago, “PIV measurements of a microchannel flow,” *Exp. Fluids* **27**, 414–419 (1999).
- ²⁸ C. Meinhart, S. Wereley, and J. Santiago, “A PIV algorithm for estimating time-averaged velocity fields,” *J. Fluids Eng.* **122**, 285–289 (2000).
- ²⁹ S. Inoué and K. Spring, *Video Microscopy*, 2nd ed. (Plenum Press, 1997).
- ³⁰ M. Olsen and R. Adrian, “Out-of-focus effects on particle image visibility and correlation in microscopic particle image velocimetry,” *Exp. Fluids* **29**, 166–174 (2000).
- ³¹ R. Keane and R. Adrian, “Optimization of particle image velocimeters. I. Double pulsed systems,” *Meas. Sci. Technol.* **1**, 1202–1215 (1990).

- ³² M. Raffel, C. Willert, S. Wereley, and J. Kompenhans, *Particle Image Velocimetry: A Practical Guide*, Mechanics (Springer-Verlag, Berlin, 2007).
- ³³ The Poiseuille slug model of a droplet in a *parallel plate* channel of height H gives non-dimensional invariants as $\Gamma^* = \frac{3}{2} \mathcal{R}$, $I^* = \frac{5\mathcal{R}}{4}$, $E^* = \frac{3\mathcal{R}}{5}$, where $\mathcal{R} = L/H$. I^* and E^* are per-unit-depth.
- ³⁴ P. Zhang and K. Mohseni, "A unified model for digitized heat transfer in a microchannel," *Int. J. Heat Mass Transfer* **78**, 393–407 (2014).
- ³⁵ A. Kloosterman, C. Poelma, and J. Westerweel, "Flow rate estimation in large depth of field micro-PIV," *Exp. Fluids* **50**, 1587–1599 (2011).
- ³⁶ C. Meyer, M. Hoffmann, and M. Schlüter, "Micro-PIV analysis of gas-liquid Taylor flow in a vertical oriented square shaped fluidic channel," *Int. J. Multiphase Flow* **67**, 140–148 (2014).
- ³⁷ The integrand of Eq. (6) can be written as $v(r_s)dr_s = v(s)\cos\beta ds$, where s is a coordinate along the interface surface, $\beta = \beta(s)$ is the angle between the radial velocity and the surface tangent vector.
- ³⁸ M. Krieg and K. Mohseni, "Modelling circulation, impulse, and kinetic energy of starting jets with non-zero radial velocity," *J. Fluid Mech.* **719**, 488–526 (2013).
- ³⁹ D. A. Fletcher and D. V. Palanker, "Pulsed liquid microjet for microsurgery," *Appl. Phys. Lett.* **78**, 1933–1935 (2001).
- ⁴⁰ X. Xia and K. Mohseni, "Axisymmetric synthetic jets: Modeling of the far-field momentum flux," in *AIAA paper, 53rd Aerospace Sciences Meeting and Exhibit*, Kissimmee, FL, 2015.
- ⁴¹ R. Li, N. Ashgriz, and S. Chandra, "Droplet generation from pulsed microjets," *Exp. Therm. Fluid Sci.* **32**, 1679–1686 (2008).
- ⁴² P. Krueger and M. Gharib, "The significance of vortex ring formation to the impulse and thrust of a starting jet," *Phys. Fluids* **15**, 1271–1281 (2003).
- ⁴³ E. Baird, P. Young, and K. Mohseni, "Electrostatic force calculation for an EWOD-actuated droplet," *Microfluid Nanofluid* **3**, 635–644 (2007).
- ⁴⁴ G. Rehbinder, "Investigation of water jet pulses generated by an impact piston device," *Appl. Sci. Res.* **40**, 7–37 (1983).
- ⁴⁵ S. Dehkoda and N. K. Bourne, "Production of a high-velocity water slug using an impacting technique," *Rev. Sci. Instrum.* **85**, 025109 (2014).
- ⁴⁶ M. Krieg and K. Mohseni, "Thrust characterization of pulsatile vortex ring generators for locomotion of underwater robots," *IEEE J. Oceanic Eng.* **33**, 123–132 (2008).
- ⁴⁷ M. Gharib, E. Rambod, and K. Shariff, "A universal time scale for vortex ring formation," *J. Fluid Mech.* **360**, 121–140 (1998).
- ⁴⁸ B. Smith and G. Swift, "A comparison between synthetic jets and continuous jets," *Exp. Fluids* **34**, 467–72 (2003).